# Suppression of the antiferromagnetic metallic state in the pressurized MnBi_{2}Te_{4} single crystal

K. Y. Chen, B. S. Wang, J.-Q. Yan, D. S. Parker, J.-S. Zhou, Y. Uwatoko, and J.-G. Cheng

Phys. Rev. Materials **3**, 094201 — Published 3 September 2019

DOI: 10.1103/PhysRevMaterials.3.094201

# Suppression of the antiferromagnetic metallic state in the pressurized $MnBi_2Te_4$ single crystal

K. Y. Chen,[1,5] B. S. Wang,[1,5,6] J.-Q. Yan,[2] D. S. Parker,[2] J.-S. Zhou,[3] Y. Uwatoko,[4] and J.-G. Cheng[1,4,5,6]*

[1]*Beijing National Laboratory for Condensed Matter Physics and Institute of Physics, Chinese Academy of Sciences, Beijing, 100190, China*

[2]*Materials Science and Technology Division, Oak Ridge National Laboratory, Oak Ridge, Tennessee 37831, USA*

[3]*Materials Science and Engineering Program, Mechanical Engineering, University of Texas at Austin, Austin, Texas 78712, USA*

[4]*Institute for Solid State Physics, University of Tokyo, 5-1-5 Kashiwanoha, Kashiwa, Chiba 277-8581, Japan*

[5]*School of Physical Sciences, University of Chinese Academy of Sciences, Beijing 100190, China*

[6]*Songshan Lake Materials Laboratory, Dongguan, Guangdong 523808, China*

E-mail: jgcheng@iphy.ac.cn

## Abstract

We study the effect of hydrostatic pressure on the electrical transport, magnetic, and structural properties of $MnBi_2Te_4$ by measuring its resistivity, Hall effect, and X-ray diffraction under pressures up to 12.8 GPa supplemented by the first-principles calculations. At ambient pressure, $MnBi_2Te_4$ shows a metallic conducting behavior with a cusp-like anomaly around $T_N \approx 24$ K where it undergoes a long-range antiferromagnetic (AF) transition. With increasing pressure, $T_N$ determined from the resistivity anomaly first increases slightly with a maximum at around 2 GPa, and then decreases until vanished completely at about 7 GPa. Intriguingly, its resistivity is enhanced gradually by pressure, and even evolves from metallic to semimetal or semiconducting-like behavior as $T_N$ is suppressed. However, the density of *n*-type charge carrier that remains dominant under pressure increases with pressure. In addition, the interlayer AF coupling seems to be strengthened under compression since the critical field $H_{c1}$ for the spin-flop transition to the canted AF state is found to increase with pressure. No structural transition was evidenced up to 12.8 GPa, but some lattice softening was observed at about 2 GPa, signaling the occurrence of an electronic transition or crossover from localized to itinerant state. We have rationalized these experimental findings by considering the pressure-induced enhancement of antiferromagnetic/ferromagnetic competition and partial delocalization of Mn-3d electrons, which not only destroys long-range AF order but also promotes charge carrier localization through enhanced spin fluctuations and/or the formation of hybridization gap at high pressure.

Keywords: $MnBi_2Te_4$, Magnetic topological insulator, Pressure effect

## Introduction

Recently, the intrinsic magnetic topological insulators have attracted tremendous research interest because they can potentially host a variety of exotic topological quantum states such as the quantum anomalous Hall effect (QAHE) and the axion insulator state.[1-3] Thanks to the theoretical predictions followed by the successful growth of sizeable single crystals, $MnBi_2Te_4$ (MBT) is a good candidate as an intrinsic magnetic topological insulator.[4-9] At ambient pressure, MBT crystallizes in the tetradymite-type structure with a rhombohedral space group *R-3m*.[10] As shown in Fig. 1, the crystal structure consists of Te-Bi-Te-Mn-Te-Bi-Te septuple layers (SLs) that are stacked along the *c*-axis. Each SL is formed by inserting a MnTe bilayer into a $Bi_2Te_3$ quintuple layer. Because these SLs are coupled through van der Waals force, atomically thin layers of MBT can be obtained by simple mechanical exfoliation. MBT thus offers a unique natural heterostructure intergrown between magnetic planes and layers of topological insulators.[11]

Transport and magnetic measurements on the MBT single crystals reveal a metallic conductivity with dominant n-type charge carriers and a long-range antiferromagnetic (AF) order below $T_N \approx 24$ K. The temperature dependence of resistivity $\rho(T)$ displays a cusp-like anomaly at $T_N$ followed by a rapid drop upon further cooling.[7, 9, 12] Refinements of powder neutron diffraction data have established an A-type AF structure consisting of antiferromagnetically coupled ferromagnetic (FM) layers with an ordered moment ~4 $\mu_B/Mn^{2+}$ pointing along the *c*-axis.[9] Because the interlayer AF coupling is relatively weak, a moderate external magnetic field $H_{c1} \sim 3.3$ T applied along the *c*-axis can induce a spin-flop transition from the A-type AF order to a canted AF (cAF) state. A state of nearly parallel spins with a saturation moment of 3.56 $\mu_B$/Mn can be induced at $H_{c2} \sim 7.8$ T.[9] As a result, the Hall resistivity $\rho_{xy}(H)$ of MBT at $T < T_N$ displays a sharp drop at $H_{c1}$ followed a weak anomaly at $H_{c2}$. Therefore, these characteristic anomalies in $\rho(T)$ and $\rho_{xy}(H)$ can be used to determine $T_N$ and $H_{c1,c2}$.

During the past few months, several important experiments have been performed on MBT. For example, Deng *et al.*[13] have observed quantized anomalous Hall effect in thin-flake samples under a moderate magnetic field, while Liu *et al.*[14] have shown a quantum phase transition from axion insulator to Chern insulator by applying magnetic field to the exfoliated flake with 6 SLs. In addition, Zheng *et al.*[15] have demonstrated a gate-controlled reversal of anomalous Hall effect in the 5-SLs MBT devices. Moreover, MBT thin films with various thickness can be grown in a well-controlled manner with molecular beam epitaxy,[16] for which both the archetypical Dirac surface state and intrinsic magnetic order have been observed.

As a layered material, the magnetic and electrical transport properties of MBT should be sensitive to interlayer and intralayer interactions, which can be tuned effectively by applying external pressures. In addition, it is possible to induce novel structural and/or

electronic phase transitions under high pressure (HP). Indeed, the HP approach has been widely employed in recent studies of topological semimetals and low-dimensional electronic materials and led to many interesting results.[17-21] We are motived in this work to investigate the effect of hydrostatic pressure on the electrical transport, magnetic, and structural properties of MBT. Interestingly, we found that the AF metallic ground state of MBT single crystal is gradually suppressed by pressure $P \geq 7$ GPa, and $\rho(T)$ even evolves to semimetal or semiconducting-like behavior. Based on the Hall resistivity measurements, detailed structural characterizations as well as first-principles calculations under HP, we proposed some possible origins responsible for these experimental findings.

## Experimental

MBT single crystals used in the present study were grown with the flux method; the detailed information about the crystal growth and characterizations can be found in Ref. 9. The HP resistivity and Hall effect were measured with standard four-probe method in a palm-type cubic anvil cell (CAC) apparatus.[22] Glycerol was used as the pressure transmitting medium (PTM). The pressure values were determined based on the pressure-loading force curve established by observing phase transitions of Bi (2.55, 2.7, 7.7 GPa) and Pb (13.4 GPa) at room temperature. It should be noted that the pressure value inside the CAC varies upon cooling, which has been characterized in our previous work.[22] The HP structural study was carried out with a diamond-anvil cell (DAC) mounted on a four-circle X-ray diffractometer (Bruker P4) with Mo anode. A small amount of NaCl (Run 1) or Au (Run 2) powder was mixed with the sample to show the pressure inside the chamber filled with Daphne 7373 as the PTM. XRD pattern was collected with an image plate from Fujifilm. We used the software FIT2D to integrate the XRD pattern into intensity versus 2θ. The unit-cell parameters were extracted from refining XRD patterns with the LeBail method.

## Results and Discussion

### HP resistivity

We performed HP resistivity measurements on two different MBT single crystals, denoted as #1 and #2 hereafter. As illustrated in the inset of Fig. 2, the current was applied within the *ab* plane in the standard four-probe resistivity measurements. Figure 2(a) shows the $\rho(T)$ curves of sample #1 under various pressures up to 12.5 GPa. At ambient pressure, $\rho(T)$ exhibits a metallic behavior in the whole temperature range and displays a cusp-like anomaly at the AF transition $T_N = 24.7$ K marked by an arrow. The rapid drop of resistivity below $T_N$ should be ascribed to the reduction of spin scattering after the formation of long-range AF order.[23] With increasing pressure, the magnitude of $\rho(T)$ is enhanced progressively and a broad hump is developed at $T > T_N$. For $P < 6$ GPa, the $\rho(T)$ curves exhibit similar behaviors characterized by a cusp-like anomaly at $T_N$ followed by a drop of resistivity below $T_N$. As shown by the

arrows in Fig. 2(a), $T_N$ determined from the resistivity anomaly first increases to ~29.6 K at 2 GPa, and then gradually decreases to ~18.3 K at 5.5 GPa. Meanwhile, the drop of resistivity below $T_N$ becomes weaker and even changes to a slight upturn at low temperatures at 5.5 GPa. For $P \geq 7$ GPa, the upturn trend becomes much stronger and no obvious anomaly can be discerned in $\rho(T)$, signaling the possible suppression of the AF order. Eventually, a semimetal or semiconducting-like behavior, *i.e.* $d\rho/dT < 0$, is realized in the high-temperature region at $P > 10$ GPa and becomes more evident with increasing pressure. It is noteworthy that the $\rho(T)$ curve at 12.5 GPa exhibits two broad humps centered at ~ 75 and 170 K, whose origin is unclear at present and requires further studies.

The run on sample #1 shows that $T_N$ reaches its maximum near 2 GPa. To confirm the variation of $T_N$ with pressure, we performed HP resistivity measurements on the sample #2. As seen in Fig. 2(b), we obtained similar results as sample #1, *i.e.* the $\rho(T)$ curves move up for $P \geq 2.5$ GPa and the $T_N$ manifested by the resistivity anomaly is suppressed gradually with increasing pressure. In comparison with sample #1, the critical pressure for the absence of resistivity anomaly at $T_N$ in sample #2 is slightly higher. The $\rho(T)$ data at 6 and 7 GPa in Fig. 2(b) illustrate more clearly how the resistivity is enhanced accompanying the suppression of AF transition to ~13 K at 7 GPa. For sample #2, we also checked resistivity after releasing pressure. As shown in Fig. 2(b), except for a slight increase of resistivity value, the sample almost recovers to its initial state with a cusp-like resistivity anomaly at $T_N$. Such a reversible pressure effect should be attributed to the excellent hydrostatic pressure condition in our CAC up to at least 15 GPa.[22] Therefore, our HP resistivity measurements reveal the concomitant suppression of AF order and development of a semiconducting-like resistivity behavior in the pressurized MBT single crystal.

### *T-P* phase diagram

Based on the above resistivity measurements, we construct a temperature-pressure phase diagram for MBT single crystal as shown in Fig. 3. A contour plot of $d\rho/dT$ based on the data set of sample #1 in Fig. 2(a) is also superimposed to highlight the evolution of the dominant conduction mechanisms. As can be seen, the AF transition temperature $T_N$ is at first slightly enhanced by pressure of ~ 2 GPa, and then suppressed gradually until vanished completely at ~7 GPa. Accompanying the suppression of AF transition, the electrical transport properties at low temperatures also change dramatically from metallic $d\rho/dT > 0$ to a semimetal or semiconducting-like behavior $d\rho/dT < 0$, as illustrated by the color coding in Fig. 3. In addition, a large $|d\rho/dT|$ manifested by the deep color in the lower part of Fig. 3 also demonstrates the changes of carrier scattering below $T_N$ in the AF metallic state at $P <$ 7 GPa and the tendency for carrier localization in the semiconducting-like state at $P >$ 7 GPa. In the paramagnetic state above $T_N$, a crossover from metallic to semiconducting behavior also takes place at higher pressures. Although pressure-

induced suppression of AF order is not unexpected, the observed monotonic enhancement of resistivity and the concomitant semiconducting-like behavior at high pressures are counterintuitive in the sense that pressure usually broadens the electronic bandwidth.

**HP Hall resistivity**

In order to gain more insights into the evolution of electronic state under pressure, we further measured Hall resistivity $\rho_{xy}(H)$ on sample #2, which was recovered from the above HP resistivity measurements. In addition to the carrier information, $\rho_{xy}(H)$ data can also provide some hints about the magnetic state through detecting the anomalies caused by the spin-flop transition mentioned above. We have measured $\rho_{xy}(H)$ at fixed temperatures of 1.5, 10, 20, and 30 K under pressures of 1, 3, 5 and 8 GPa. The measurement configuration is schematically shown in the inset of Fig. 4(a), in which the current was applied within the *ab* plane and the magnetic field applied along the *c*-axis. The $\rho_{xy}(H)$ data collected for a field sweeping between +8.5 and -8.5 T are anti-symmetrized in order to eliminate the contributions from the longitudinal magnetoresistance.

Some representative $\rho_{xy}(H)$ data at 1.5 K ($< T_N$) and 30 K ($> T_N$) under different pressures are shown in Fig. 4(a, b). All $\rho_{xy}(H)$ curves display an initial negative slope, suggesting that the electron-type carriers dominate the transport properties up to at least 8 GPa. For $T = 1.5$ K, Fig. 4(a), $\rho_{xy}(H)$ at 1 GPa exhibits a gradual drop starting at 4.8 T and ending at 5.3 T due to the field-induced spin-flop transition from AF to cAF. In comparison with a much sharper drop of $\rho_{xy}(H)$ at $H_{c1} \sim 3.3$ T under ambient pressure,[9] the spin-flop transition at 1 GPa takes place at a larger magnetic field. This observation indicates that the interlayer AF coupling is strengthened due to the reduction of *c*-axis. This is also consistent with the enhancement of $T_N$ at $P \leq 2$ GPa in Fig. 3. As a result, we cannot detect the cAF to FM transition in $\rho_{xy}(H)$ up to 8.5 T, the highest field in our measurements.

When increasing pressure to ≥ 3 GPa, the initial slope of $\rho_{xy}(H)$ decreases and keeps nearly constant, implying an enhanced carrier density as discussed below. For $P = 3$ GPa, the spin-flop transition occurs at much higher field of $H_{c1} \geq 7$ T, and becomes much more broaden than that at 1 GPa. The continuous increase of $H_{c1}$ at 3 GPa would suggest a further enhancement of interlayer AF coupling and thus $T_N$. However, the observed reduction of $T_N$ at 3 GPa in Figs. 2 and 3 implies that some other competing factors are at play under HP. As discussed below, the enhanced intralayer AF/FM competition and the reduction of Mn magnetic moment should be responsible for the suppression of $T_N$ above 3 GPa. For $P = 5$ and 8 GPa, $\rho_{xy}(H)$ curves are perfect linear without any anomaly up to 8.5 T. Further studies in a larger field range are needed to address whether the spin-flop transition would take place at a field higher than 8.5 T or disappear gradually when the intra- and inter-layer AF interactions become stronger. For $T = 30$ K, Fig. 4(b), all $\rho_{xy}(H)$ curves are linear in field up to 8.5

T and the negative slope is reduced gradually with increasing pressure.

We have extracted the Hall coefficient $R_H$ from a linear fitting to the $\rho_{xy}(H)$ curves in the linear region as indicated by the dotted lines in Fig. 4(a, b). The obtained $R_H(P)$ at 1.5 and 30 K are plotted in Fig. 4(c). For both temperatures, $|R_H(P)|$ first decreases quickly with increasing pressure and then tends to level off above 3 GPa. This observation indicates that the influence of pressure on the electronic state is moderate for $P > 3$ GPa. Based on a single-band model, we estimated the carrier density $n = -(eR_H)^{-1}$ and mobility $\mu = R_H/\rho$, which are displayed in Fig. 4(d, e). At 1.5 K, the obtained carrier density at 1 GPa ~$1.2\times10^{20}$ cm$^{-3}$ is slightly large than that of ~ 0.9 $\times10^{20}$ cm$^{-3}$ at ambient pressure,[9] and is further increased to ~$1.8\times10^{20}$ cm$^{-3}$ above 3 GPa. The carrier density at 30 K also increases progressively from $0.94\times10^{20}$ cm$^{-3}$ at 1 GPa to $2.16\times10^{20}$ cm$^{-3}$ at 8 GPa. Since the carrier density is improved by pressure, the observed continuous increase of resistivity and the semiconducting-like behavior at low temperature and higher pressures cannot be attributed to suppression of bulk carriers or the opening of bulk band gap. Instead, it should be ascribed to the significant reduction of carrier mobility shown in Fig. 4(e). As discussed below, the carrier localization might be correlated with the enhanced magnetic fluctuations accompanying the suppression of AF order.

It is also noteworthy that $R_H(P)$ at 1.5 and 30 K are crossed at 5 GPa as illustrated by opposite directions of the vertical arrows in Fig. 4(c). This fact reflects the distinct electronic states of MBT at low and high pressures. As shown in Fig. 4(g), the carrier density $n(T)$ at 1 GPa experiences a sudden enhancement below ~ 20 K, corresponding to the rapid drop of resistivity below $T_N$ in Fig. 2. A similar feature is still visible at 3 and 5 GPa, but it becomes much weaker, which is also consistent with the diminishing resistivity drop below $T_N$. In contrast, $n(T)$ at 8 GPa monotonically decreases upon cooling, which also explains the observed resistivity upturn or semiconducting-like behavior at low temperatures under $P > 7$ GPa. Therefore, these systematic investigations on the HP Hall resistivity further elaborate a pressure-induced electronic transition or crossover in MBT single crystal.

**HP structural study**

Before discussing the possible origins for these observations, we first investigated the structural responses under pressure. No obvious sudden changes were observed in the above HP resistivity measurements during the compression process, implying the absence of pressure-induced structural transition at least up to 12.5 GPa. In order to confirm this, we performed HP XRD measurements at room temperature. During the measurements, we found that the fine powder sample from the pulverized crystals gives very weak and broad peaks. So, we used clusters of small crystals for the HP XRD measurements, and carried out two separated runs to check the reproducibility. In this case, these clusters rotate inside the gasket hole with the preference of *c*-axis normal to the anvil surfaces. As such, the sample should experience stronger uniaxial

strain along the *c*-axis than the *ab* plane at higher pressures where the pressure medium is solidified.

Figure 5(a) shows the XRD patterns of MBT up to 12.8 GPa for the first run (Run 1). The observation of similar patterns confirms the absence of structural phase transition in the investigated pressure range. The XRD patterns of the second run (Run 2, not shown here) look identical with Run 1, further verifying the stability of crystal structure. It should be noted that some peaks become rather weak under pressure due to the development of preferred orientation for the reason mentioned above.

The lattice parameters, *a*, *c*, and *V*, extracted from these XRD patterns with the LeBail method are displayed in Fig. 5(b, c, d) as a function of pressure. As can be seen, the results from these two runs are generally consistent with each other, and all lattice parameters decrease monotonically without showing clear discontinuity, in line with the absence of structural transition under HP. In contrast to the well matched lattice parameter *a* for these two runs, however, some discrepancies are present for *c* (and thus *V*) above 2 GPa, which should reflect the different *c*-axis uniaxial stress experienced by the samples in these two runs. The design of a DAC is to press a thin disk-shape chamber along the axis normal to the disk. As the pressure medium is solidified at a high pressure, the loading force produces more stress along the axis than in lateral directions. Given the preferred crystal orientation of a MBT crystal in the chamber, crystal grains experience higher stress along the *c*-axis than in the *ab* plane. Nevertheless, Run 2 with dense pressure points reveal a clear slope change for the lattice parameter *c* at ~ 2 GPa and 7.5 GPa. On crossing 2 GPa, the lattice parameters become more compressible. Such a lattice softening may suggest a pressure-induced electronic transition or crossover from localized to itinerant-electron behavior as seen in other systems.[24, 25] As discussed below, this anomaly in lattice parameters versus pressure is consistent with the reduced Mn moment under pressure from first-principles calculations and can also rationalize the non-monotonic change of $T_N(P)$. The *c* axis becomes less compressible for $P > 7.5$ GPa where the magnetism disappears.

As shown in Fig. 5(b, c), the unit cell experiences a strong anisotropic compression, *i.e.* $\Delta a/a_0 = -4.77$ % versus $\Delta c/c_0 = -8.91$ %, up to 12.8 GPa. This is mainly due to the layered structure of MBT with weak van der Waals force along the *c*-axis. Under the circumstance of no pressure-induced phase transition, the pressure dependence of cell volume can be described with the Birch-Murnaghan (B-M) equation, *i.e.*

$$P = \frac{3B_0}{2}\left[\left(\frac{V_0}{V}\right)^{7/3} - \left(\frac{V_0}{V}\right)^{5/3}\right]\left\{1 + \frac{3}{4}(B'-4)\left[\left(\frac{V_0}{V}\right)^{2/3} - 1\right]\right\} \quad (1).$$

But the presence of preferred orientation and the uniaxial strain make it difficult to obtain reliable fitting results for the layered materials like MBT. The best fit to $V(P)$ of Run 1 yields a bulk modulus $B_0 = 32.0 \pm 3.0$ GPa, $B' = 7.7 \pm 0.9$, and $V_0 = 665.2 \pm$

2.5 Å$^3$, respectively. The obtained values of $B_0$ and $B'$ for MBT are close to those of $SnBi_2Te_4$, *i.e*. $B_0$ = 35(2) GPa and $B'$ = 6.2(7).[26] Note that if $B'$ = 4 is fixed, we obtain a larger $B_0$ = 46.6 ± 1.9 GPa and smaller $V_0$ = 658.0 ± 2.8 Å$^3$, which is not consistent with the volume at ambient pressure. The result of fitting $V(P)$ in Run 2 to the B-M equation is quite poor over the entire pressure range in this experiment. But different $B_0$ values of 62.1 ± 7.4, 33.4 ± 1.3, and 55.4± 2.3 with $B'$ = 4 fixed can be obtained when the fitting was performed in three pressure ranges $0 < P < 2$, $2 < P < 7.5$, and $7.5 < P < 11$ GPa.

**First-principles calculations**

For a better understanding of these experimental findings, we have performed first-principles calculations using the augmented plane-wave all-electron code WIEN2K [27] within the generalized gradient approximation of Perdew, Burke and Ernzerhof.[28] These calculations were conducted at the unit-cell parameters corresponding to ambient pressure, 7 GPa, and an effective pressure of ~20 GPa with $a$ = 4 Å and $c$ = 36 Å, respectively. Here we have chosen a rather large pressure as a sensitive check on the calculations because it is well known that the suppression of magnetic order by pressure is often underestimated by first-principles approaches.

At ambient pressure, we find the A-type AF state to fall ~7 meV per Mn below the FM configuration, in agreement with the experimental result.[9] Figure 6 shows the calculated density of states (DOS) for MBT in the AF ground state at ambient pressure. As can be seen, a small band gap of ~ 0.07 eV, which is very likely underestimated in GGA, is obtained for these calculations with spin-orbit coupling. In addition, we observe a substantial exchange splitting of ~ 4 eV between the peaks of DOS for the majority spin Mn1 and minority spin Mn2. As in several other anisotropic compounds, the overall exchange splitting is large despite of a small interlayer exchange coupling accounting for the ordering temperature of just 24 K. The DOS for both Mn atoms are relatively localized and the majority of the Mn1 spin-up DOS is about 3 eV below the valence band maximum, which reflects the robust moment formation in MBT. The calculated Mn staggered moment is about 4.29 $\mu_B$ for the A-type AF state. Similar characteristics were also found for MnTe,[29] even though the interlayer exchange coupling and consequently Néel temperature in MnTe are much larger. On the other hand, a metallic behavior is obtained in a non-spin-polarized calculation.

It is noteworthy that the degree and character of the hybridization is very different for the valence and the conduction bands. As seen in Fig. 6, the majority of DOS in the first 2 eV below the valence band maximum has the Te character, mixed with some component of Mn1 near the band edge. In contrast, the largest portion of DOS in the conduction band comes from the minority spin Mn2, in addition to some significant contributions from both Bi and Te. A similar situation prevails in $Bi_2Te_3$ itself,[30] but there the hybridization in the valence band is significantly stronger than that in the

conduction band. The substantial difference in their electronic structures underscores the great influence of the Mn magnetism on the properties here, even though Mn only comprises 1/7$^{th}$ of the atoms in the crystal structure.

With the application of 7 GPa pressure, the calculated staggered moment is slightly reduced to 4.12 $\mu_B$, and the AF state shows a semi-metallic behavior with a band overlap of about 50 meV. At the assumed 20 GPa pressure, however, we find a much more substantial reduction in magnetic order, with a calculated moment of 3.59$\mu_B$. Note a small fraction of this reduction is due to the use of smaller "muffin-tin" radii, within which the Mn spin moment is calculated, in this highly compressed unit cell. This larger reduction is qualitatively consistent with the observed suppression of magnetic order by pressure, and supports the scenario of localized-itinerant crossover according to the HP structural results. Note that we have not assessed the effects of pressure on the exchange interactions ultimately determining the ordering point. Similar with the 7 GPa case, we find a metallic behavior at 20 GPa with a much larger band overlap of ~300 meV. The increased band overlap seen from calculations is consistent with the observed enhancement of carrier density seen in Fig. 4(d).

The theoretical prediction of metallic behavior under applied pressure, but semiconducting behavior at ambient pressure, seems to contradict the experimental transport results that show the reverse. However, there are numerous complications affecting the comparison between theory and experiment. First and foremost, the disappearance of long-range AF order at $T_N$ does not necessarily signal the loss of all magnetic character. In addition, for a highly anisotropic material such as MBT with large local moment, it is also likely that local magnetic correlations persist well above the nominal ordering point.[31] Such behavior is evident in numerous other 3*d*-based magnetic materials, such as $Mn_3Si_2Te_6$ [32] and $LiGaCr_4S_8$ [33], where magnetism-related semiconducting behavior persists to temperatures well above the long-range ordering temperature. Although the complex behavior of the observed resistivity with pressure most likely originates in all these factors, further experimental and theoretical study will be needed to develop a detailed understanding.

**Discussion**

The main experimental findings of the present HP study on MBT can be summarized as follow: (1) $T_N$ for the A-type AF order exhibits a positive ( $P < 2$ GPa) and then negative ($P > 2$ GPa) pressure effect until vanishes at ~ 7 GPa; (2) the resistivity is unusually enhanced by pressure and even shows a non-metallic behavior as $T_N$ is suppressed completely; (3) the band structure remains robust against pressure with n-type charge carriers dominating the transport properties, and the carrier density increases with pressure; (4) the interlayer AF coupling is strengthened by pressure due to the reduction of *c*-axis; (5) no structural phase transition takes place below 12.8 GPa, albeit the lattice parameters show an anomalous change around 2 GPa, presumably driven by an electronic transition from localized to itinerant behavior.

Although first-principles calculations here cannot explain all experimental results, the obtained band structure and the evolution of Mn magnetism provide some bases for us to understand these observations.

Since our HP XRD measurements rule out the structural transition in the investigated pressure range, the observed suppression of AF metallic state should be caused by electronic state changes induced by lattice compression. As indicated by the results of Hall coefficient measurement, the carrier density is actually raised by pressure; thus the enhancement of resistivity under pressure cannot be explained by the suppression of bulk carrier or band gap opening. Alternatively, the charge carriers seem to experience a strong tendency for localization, which should correlate closely with the evolution of magnetism. This is supported by the fact that both the development of resistivity upturn at low temperatures and the semiconducting-like behavior in the high-temperature region at $P > 7$ GPa are accompanied with the suppression of long-range AF order. Thus, the essential point is to understand the pressure dependence of $T_N$ and the correlation between magnetism and electrical transport properties.

As mentioned above, the increase of $H_{c1}$ under pressure, Fig. 4(a), suggests that the interlayer AF coupling between the FM layers is strengthened due to the reduction of *c*-axis under compression, which can explain the initial increase of $T_N$. Under the hydrostatic pressure conditions, both *a* and *c* axes are compressed, and thus both intra- and inter-layer magnetic interactions are expected to be modified accordingly. It has been proposed in the $MnBi_{2-x}Sb_xTe_4$ that the reduced nearest-neighbor Mn-Mn distance within the *ab* plane upon Sb doping would increase the direct AF interactions that compete with the dominant intralayer FM interactions.[34] In the present case, HP should also enhance the intralayer direct AF interactions, which can compete with the dominant FM interactions. Such an AF/FM competition in a localized-moment picture is expected to lower $T_N$ of this A-type AF phase. On the other hand, the observed lattice softening starting at ~ 2 GPa shown in Fig. 5(c, d) is consistent with an electronic crossover from localized to itinerant state, *i.e.* the lattice is more compressible on the itinerant-electron side.[24, 25] This should primarily take place on the Mn-3d electrons, which can undergo a partial delocalization above 2 GPa. The localized-itinerant crossover at 2 GPa can also rationalize the broad maximum of $T_N$ shown in Fig. 3, because $T_N$ associated with the localized- and itinerant-electrons shows opposite pressure dependencies.[24] Such a scenario is also supported by the first-principles calculations, which show that the magnetic moment of Mn ions is reduced gradually with increasing pressure. Taking into account these factors together, the increase of $T_N$ with pressure below 2 GPa can be rationalized by a picture of localized electron where the perturbation expression of superexchange interaction remains valid, whereas both the enhanced AF/FM magnetic competition and the partial delocalization of Mn moments under pressure should be responsible for the suppression of $T_N$ above 2 GPa.

Accordingly, two mechanisms can be invoked to explain the unusual increase of resistivity under pressure. On the one hand, the suppression of long-range AF is expected to enhance the magnetic fluctuations, which can increase the electron scattering, in consistent with the reduced carrier mobility shown in Fig. 4(e), and promote charge carrier localization in an itinerant-electron system. This effect indeed becomes much stronger at $P > 7$ GPa when the long-range AF order disappears completely. As such, this scenario ends up with a semiconducting-like behavior in resistivity through a magnetic fluctuation induced carrier localization process, even though the magnitude of resistivity remains in the semimetal or bad-metal regime. Similar resistivity behavior has been observed in the geometrically frustrated AF pyrochlore $Ca_2Ru_2O_7$ due to the interplay between frustrated magnetism and the itinerant electrons.[35] On the other hand, the partial delocalization of Mn-3d electrons would promote its hybridization with the Bi-6p and/or Te-5p conduction electrons, Fig. 6, which might give rise to a hybridization gap as found in $CaMn_2Bi_2$.[36] In the latter compound, its resistivity displays a metallic behavior at high temperatures but changes to activated behavior at low temperatures.[36] Band-structural calculations suggest that one of the Mn-$3d^5$ electrons strongly hybridizes with the Bi-6p bands giving rise to a hybridization gap, while the other d electrons remain localized to give an ordered moment of 3.85 $\mu_B$ at 5 K. A recent HP resistivity measurements on $CaMn_2Bi_2$ has shown that its resistivity and the activation gap are both increased by pressure, in support of the hybridization-gap semiconductor behavior.[37] Similar situations observed in MBT, including a comparable moment of ~ 4.04 $\mu_B$/Mn,[9] substantial hybridization between Mn-d and Bi-p states in band structures (Fig. 6), and the enhancement of resistivity under pressure (Fig. 2), indicate that MBT might become a hybridization-gap semiconductor. Further studies are needed to verify such a scenario.

Finally, our present results on MBT might provide some implications for the optimization of its topological properties. For an ideal magnetic topological insulator, it is essential to achieve an insulating bulk state, while existing MBT single crystals are metallic with dominated n-type carriers.[9, 38] In addition, single crystals were found to contain Mn/Bi anti-site disorders and/or Mn vacancies, which can alter the transport properties significantly.[7, 12] For thin flakes, the gate-voltage tuning has been applied to suppress the bulk carriers and to tune the Fermi level into the surface band gap so as to observe the quantum phase transitions.[14] On the other hand, substitutions of Sb for Bi in the series of $Mn(Sb_xBi_{1-x})_2Te_4$ have also been attempted to open the bulk band gap through shifting the Fermi level.[34, 38] Although a transition from n-to-p type charge carriers has been observed, the metallic conduction remains prevailing in the series of $Mn(Bi_{1-x}Sb_x)_2Te_4$. In contrast, our $\rho(T)$ data at HP resemble those of the gate-voltage-tuned thin flakes with the Fermi level lying inside the surface band gap.[14] Our present work thus indicates that an insulating bulk state might be achievable in MBT thin films under compressive epitaxy strain at ambient pressure.

## Conclusion

In summary, we have performed a comprehensive HP study on the MBT single crystal, which is considered as the first intrinsic AF topological insulator. We find that its resistivity is gradually enhanced by pressure and even changes from metallic to semiconducting-like behavior at $P$ >7 GPa. In addition, we found that the AF transition was initially strengthened due to the reduction of interlayer distances, but then suppressed gradually until vanished completely at ~ 7 GPa. The layered structure of MBT is confirmed to preserve at pressures up to at least 12.8 GPa. We have discussed our experimental findings in terms of the competing magnetic interactions and localized-to-itinerant crossover based on the results of Hall resistivity, structural characterizations, and first-principles calculations under HP. Our results call for further experimental and theoretical studies on MBT in order to achieve a better understanding on the interplay between magnetism and transport properties.

## Acknowledgements

This work is supported by the National Key R&D Program of China (Grant Nos. 2018YFA0305700 and 2018YFA0305800), the National Natural Science Foundation of China (Grant Nos. 11574377, 11888101, 11834016, 11874400), the Strategic Priority Research Program and Key Research Program of Frontier Sciences of the Chinese Academy of Sciences (Grant Nos. XDB25000000 and QYZDB-SSW-SLH013), as well as the CAS Interdisciplinary Innovation Team. JQY and DSP are supported by the US Department of Energy, Office of Science, Basic Energy Sciences, Materials Sciences and Engineering Division. J.S.Z. is supported by the National Science Foundation DMR-1729588.

## References

1 R. S. K. Mong, A. M. Essin, and J. E. Moore, Phys. Rev. B **81**, 245209 (2010).

2 J. Li, Y. Li, S. Du, Z. Wang, B.-L. Gu, S.-C. Zhang, K. He, W. Duan, and Y. Xu, Sci. Ad. **5**, eaaw5685 (2019).

3 D. Zhang, M. Shi, T. Zhu, D. Xing, H. Zhang, and J. Wang, Phys. Rev. Lett. **122**, 206401 (2019).

4 M. M. Otrokov, T. V. Menshchikova, M. G. Vergniory, I. P. Rusinov, A. Yu Vyazovskaya, Y. M. Koroteev, G. Bihlmayer, A. Ernst, P. M. Echenique, A. Arnau, and E. V. Chulkov, 2D Mater. **4**, 025082 (2017).

5 M. M. Otrokov, T. V. Menshchikova, I. P. Rusinov, M. G. Vergniory, V. M. Kuznetsov, and E. V. Chulkov, JETP Lett. **105**, 297 (2017).

6 M. M. Otrokov, I. I. Klimovskikh, H. Bentmann, A. Zeugner, Z. S. Aliev, S. Gass, A. U. B. Wolter, A. V. Koroleva, D. Estyunin, A. M. Shikin, M. Blanco-Rey, M. Hoffmann, A. Y. Vyazovskaya, S. V. Eremeev, Y. M. Koroteev, I. R. Amiraslanov, M. B. Babanly, N. T. Mamedov, N. A. Abdullayev, V. N. Zverev, B. Büchner, E. F. Schwier, S. Kumar, A. Kimura, L. Petaccia, G. Di Santo, R.

C. Vidal, S. Schatz, K. Kißner, C.-H. Min, S. K. Moser, T. R. F. Peixoto, F. Reinert, A. Ernst, P. M. Echenique, A. Isaeva, and E. V. Chulkov, arXiv:1809.07389 (2018).

7 A. Zeugner, F. Nietschke, A. U. B. Wolter, S. Gaß, R. C. Vidal, T. R. F. Peixoto, D. Pohl, C. Damm, A. Lubk, R. Hentrich, S. K. Moser, C. Fornari, C. H. Min, S. Schatz, K. Kißner, M. Ünzelmann, M. Kaiser, F. Scaravaggi, B. Rellinghaus, K. Nielsch, C. Hess, B. Büchner, F. Reinert, H. Bentmann, O. Oeckler, T. Doert, M. Ruck, and A. Isaeva, Chem. Mater. **31**, 2795 (2019).

8 M. M. Otrokov, I. P. Rusinov, M. Blanco-Rey, M. Hoffmann, A. Y. Vyazovskaya, S. V. Eremeev, A. Ernst, P. M. Echenique, A. Arnau, and E. V. Chulkov, Phys. Rev. Lett. **122**, 107202 (2019).

9 J. Q. Yan, Q. Zhang, T. Heitmann, Z. Huang, K. Y. Chen, J. G. Cheng, W. Wu, D. Vaknin, B. C. Sales, and R. J. McQueeney, Phys. Rev. Mater. **3**, 064202 (2019).

10 D. S. Lee, T.-H. Kim, C.-H. Park, C.-Y. Chung, Y. S. Lim, W.-S. Seo, and H.-H. Park, Cryst. Eng. Comm. **15**, 5532 (2013).

11 S. V. Eremeev, M. M. Otrokov, and E. V. Chulkov, Nano Lett. **18**, 6521 (2018).

12 J. Cui, M. Shi, H. Wang, F. Yu, T. Wu, X. Luo, J. Ying, and X. Chen, Phys. Rev. B **99**, 155125 (2019).

13 Y. Deng, Y. Yu, M. Zhu Shi, J. Wang, X. H. Chen, and Y. Zhang, ArXiv:1904.11468 (2019).

14 C. Liu, Y. Wang, H. Li, Y. Wu, Y. Li, J. Li, K. He, Y. Xu, J. Zhang, and Y. Wang, arXiv:1905.00715 (2019).

15 S. Zhang, R. Wang, X. Wang, B. Wei, H. Wang, G. Shi, F. Wang, B. Jia, Y. Ouyang, B. Chen, Q. Liu, F. Xie, F. Fei, M. Zhang, X. Wang, D. Wu, X. Wan, F. Song, H. Zhang, and B. Wang, arXiv:1905.04839 (2019).

16 Y. Gong, J. Guo, J. Li, K. Zhu, M. Liao, X. Liu, Q. Zhang, L. Gu, L. Tang, X. Feng, D. Zhang, W. Li, C. Song, L. Wang, P. Yu, X. Chen, Y. Wang, H. Yao, W. Duan, Y. Xu, S.-C. Zhang, X. Ma, Q.-K. Xue, and K. He, Chin. Phys. Lett. **36**, 076801 (2019).

17 Y. Zhou, P. Lu, Y. Du, X. Zhu, G. Zhang, R. Zhang, D. Shao, X. Chen, X. Wang, M. Tian, J. Sun, X. Wang, Z. Yang, W. Yang, Y. Zhang, and D. Xing, Phys. Rev. Lett. **117**, 146402 (2016).

18 Y. Zhou, J. Wu, W. Ning, N. Li, Y. Du, X. Chen, R. Zhang, Z. Chi, X. Wang, X. Zhu, P. Lu, C. Ji, X. Wang, Z. Yang, J. Sun, W. Yang, M. Tian, Y. Zhang, and H.-K. Mao, PNAS **113**, 2904 (2016).

19 P. L. Cai, J. Hu, L. P. He, J. Pan, X. C. Hong, Z. Zhang, J. Zhang, J. Wei, Z. Q. Mao, and S. Y. Li, Phys. Rev. Lett. **115**, 057202 (2015).

20 M. Yankowitz, S. Chen, H. Polshyn, Y. Zhang, K. Watanabe, T. Taniguchi, D. Graf, A. F. Yong, and C. R. Dean, Science **363**, 1059 (2019).

21 F. Ke, Y. Chen, K. Yin, J. Yan, H. Zhang, Z. Liu, J. S. Tse, J. Wu, H.-K. Mao,

and B. Chen, PNAS **116**, 9186 (2019).

22 J.-G. Cheng, K. Matsubayashi, S. Nagasaki, A. Hisada, T. Hirayama, M. Hedo, H. Kagi, and Y. Uwatoko, Rev. Sci. Instru. **85**, 093907 (2014).

23 M. E. Fisher and J. S. Langre, Phys. Rev. Lett. **20**, 665 (1968).

24 J.-S. Zhou and J. B. Goodenough, Phys. Rev. Lett. **89**, 087201 (2002).

25 J.-S. Zhou, C.-Q. Jin, Y.-W. Long, L.-X. Yang, and J. B. Goodenough, Phys. Rev. Lett. **96**, 046408 (2006).

26 R. Vilaplana, J. A. Sans, F. J. Manjón, A. Andrada-Chacón, J. Sánchez-Benítez, C. Popescu, O. Gomis, A. L. J. Pereira, B. García-Domene, P. Rodríguez-Hernández, A. Muñoz, D. Daisenberger, and O. Oeckler, J. Alloy. Compound. **685**, 962 (2016).

27 P. Blaha, K. Schwarz, G. K. H. Madsen, D. Kvasnicka, and J. Luitz, htt://www.wien2k.at (2001).

28 J. P. Perdew, K. Burke, and M. Ernzerhof, Phys. Rev. Lett. **77**, 3865 (1996).

29 D. S. Parker, Unpublished.

30 A. Hashibon and C. Elsässer, Phys. Rev. B **84**, 144117 (2011).

31 F. J. Pinski, J. Staunton, B. L. Gyorffy, D. D. Johnson, and G. M. Stocks, Phys. Rev. Lett. **56**, 2096 (1986).

32 A. F. May, Y. Liu, S. Calder, D. S. Parker, T. Pandey, E. Cakmak, H. B. Cao, J. Q. Yan, and M. A. McGuire, Phys. Rev. B **95**, 174440 (2017).

33 G. Pokharel, A. F. May, D. S. Parker, S. Calder, G. Ehlers, A. Huq, and S. A. e. a. Kimber, Phys. Rev. B **97**, 134117 (2018).

34 J.-Q. Yan, S. Okamoto, M. A. McGuire, A. F. May, R. J. McQueeney, and B. C. Sales, arXiv:1905.00400 (2019).

35 T. Munenaka and H. Sato, J. Phys. Soc. Jpn. **75**, 103801 (2006).

36 Q. D. Gibson, H. Wu, T. Liang, M. N. Ali, N. P. Ong, Q. Huang, and R. J. Cava, Phys. Rev. B **91**, 085128 (2015).

37 M. M. Piva, S. M. Thomas, Z. Fisk, J.-X. Zhu, J. D. Thompson, P. G. Pagliuso, and P. F. S. Rosa, Phys. Rev. B **100**, 045108 (2019).

38 B. Chen, F. Fei, D. Zhang, B. Zhang, W. Liu, S. Zhang, P. Wang, B. Wei, Y. Zhang, J. Guo, Q. Liu, Z. Wang, X. Wu, J. Zong, X. Xie, W. Chen, Z. Sun, D. Shen, S. Wang, Y. Zhang, M. Zhang, F. Song, H. Zhang, and B. Wang, arXiv:1903.09934 (2019).

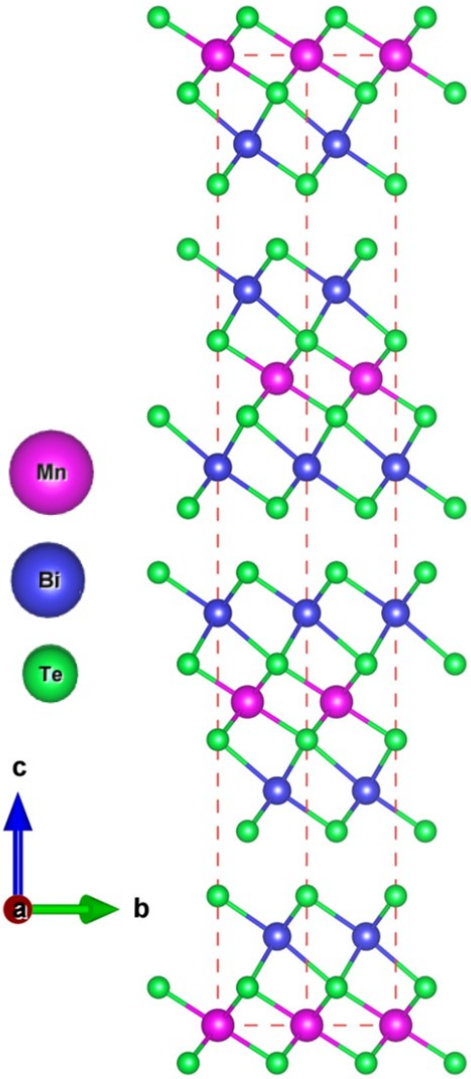


Figure 1. Crystal structure of $MnBi_2Te_4$.

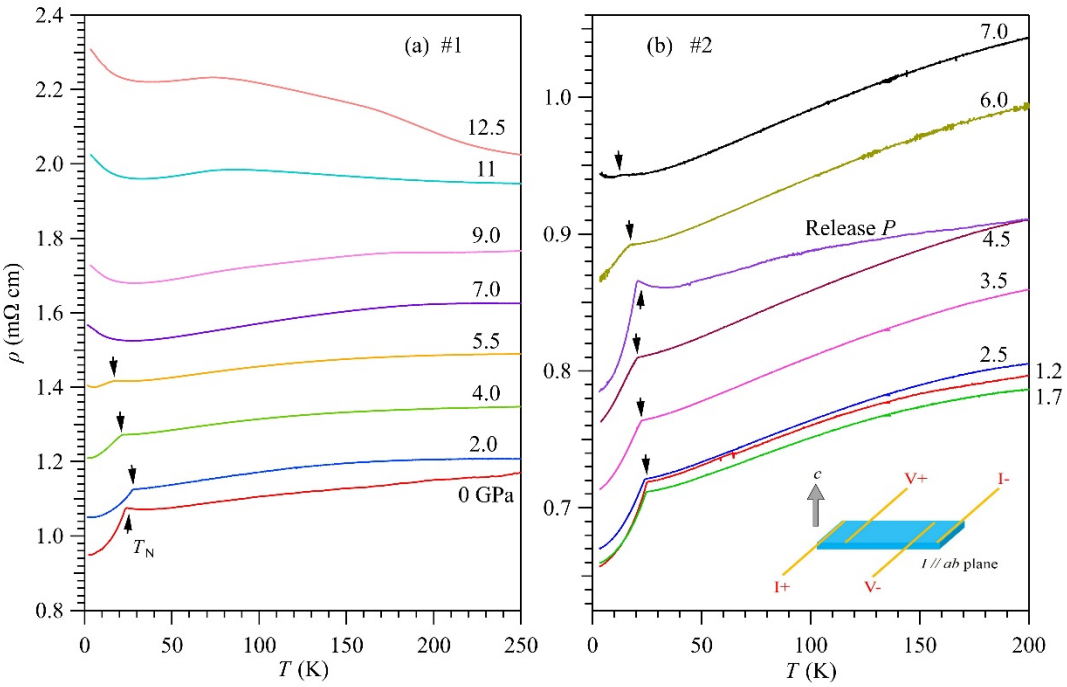


Figure 2. Temperature dependence of resistivity $\rho(T)$ for $MnBi_2Te_4$ under various pressures (a) up to 12.5 GPa for sample #1 and (b) up to 7 GPa for sample #2. The Neel temperature $T_N$ is marked by the black arrow. Inset of Fig. 1(b) displays the configuration for resistivity measurements under HP.

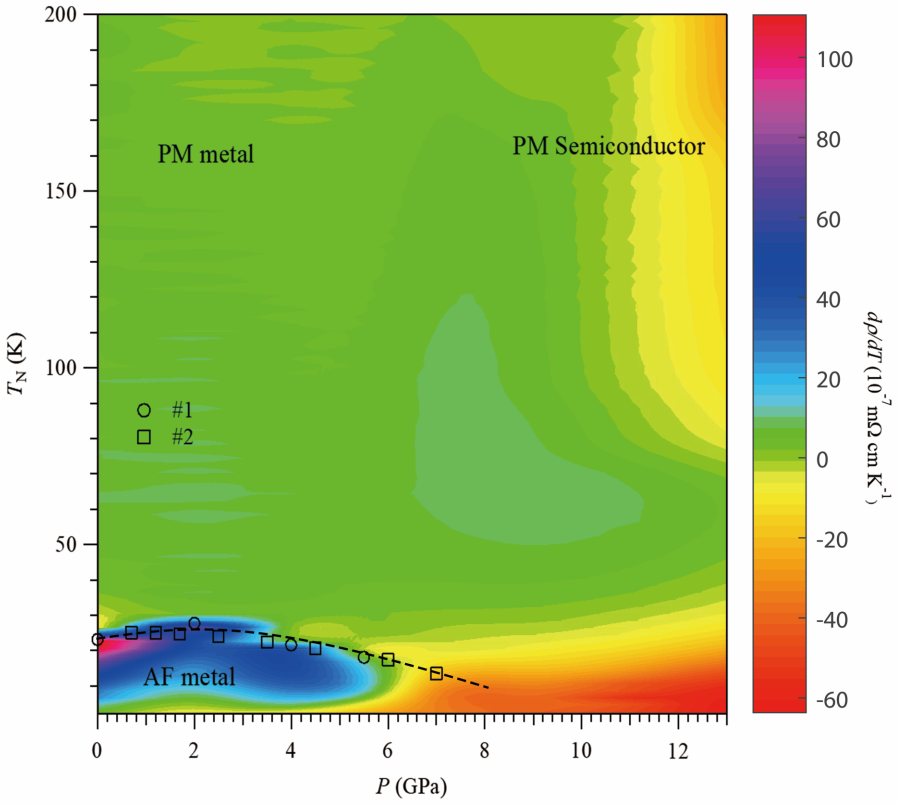


Figure 3. Temperature-pressure phase diagram of $MnBi_2Te_4$.

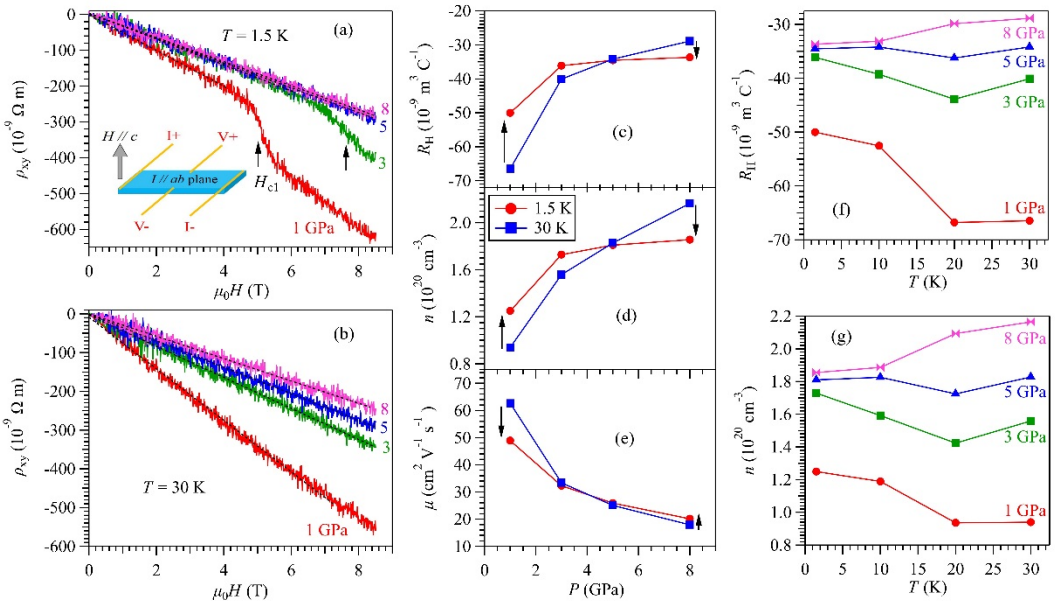


Figure 4. (a, b) Field dependence of Hall resistivity $\rho_{xy}(H)$ of MBT #2 at 1.5 K and 30 K under different pressures. (c, d, e) Pressure dependences of Hall coefficient $R_H$, carrier density $n$, and mobility $\mu$ at 1.5 and 30 K. (f, g) Temperature dependences of $R_H$ and $n$ at different pressures. Inset of Fig. 4(a) displays the configuration for Hall resistivity measurements under HP.

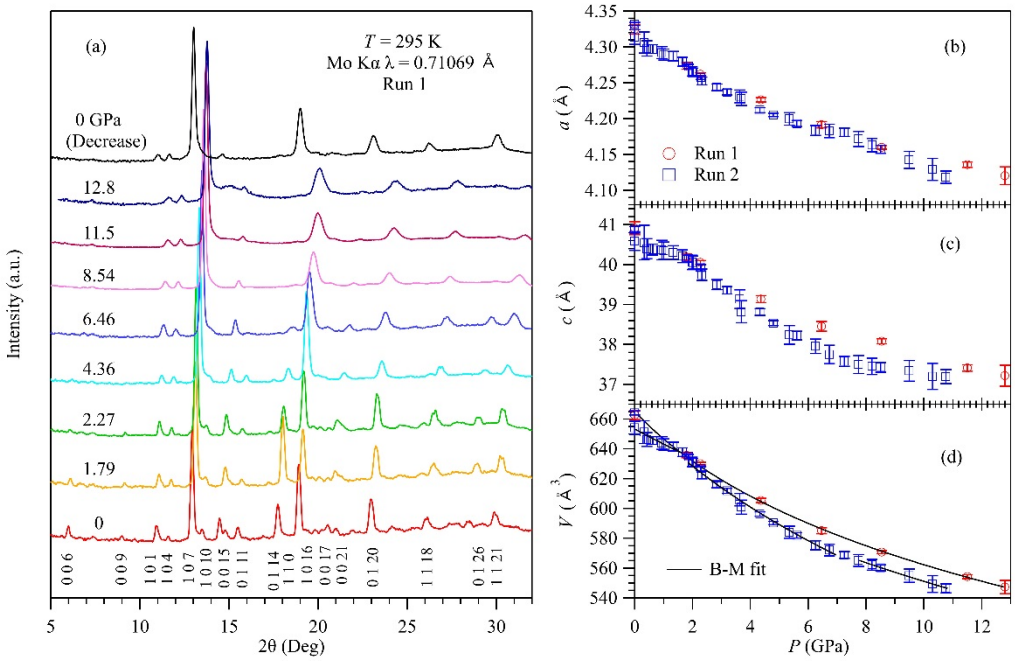


Figure 5. (a) Powder XRD patterns of $MnBi_2Te_4$ up to 12.8 GPa at Run 1, (b, c, d) Pressure dependences of the unit-cell parameters $a$, $c$, and $V$ for two runs. The solid lines in (d) are B-M fitting curves.

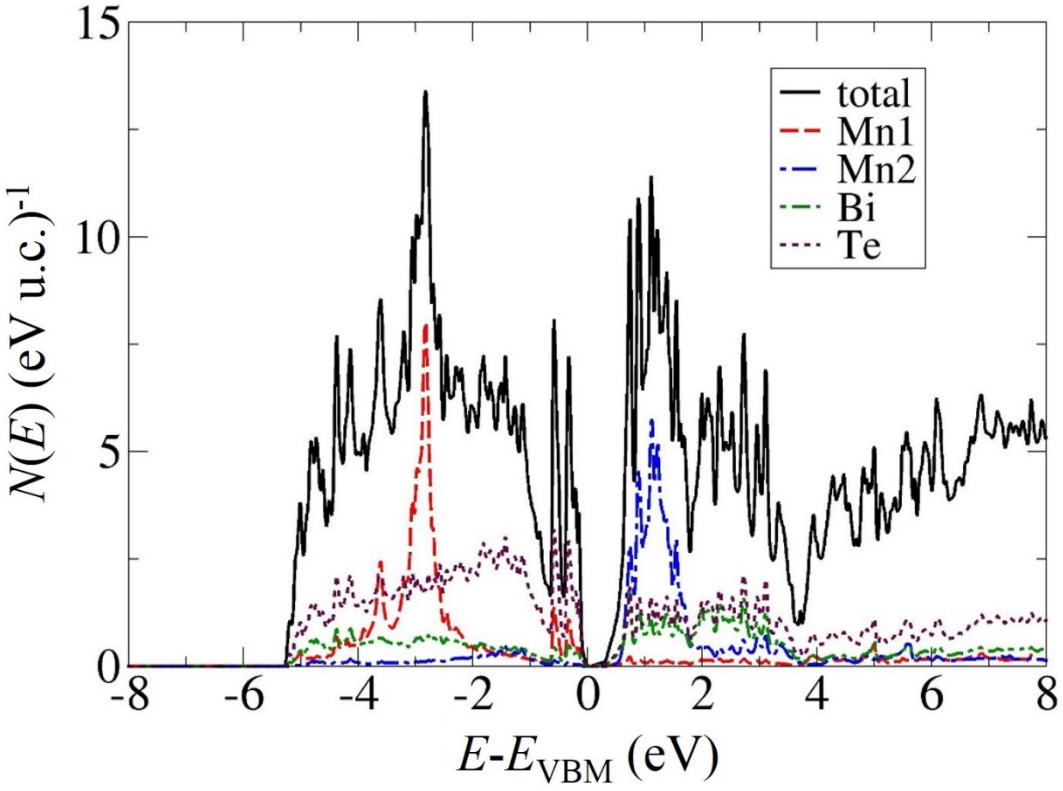


Figure 6. The calculated density of states (DOS) of $MnBi_2Te_4$ in the AF ground state at ambient pressure. For clarity only the spin-up DOS is shown; the spin-down DOS is essentially identical except that the Mn1 and Mn2 DOS are reversed.